Formation of three-dimensional quantum-dot superlattices in amorphous systems: Experiments and Monte Carlo simulations

M. Buljan, U. V. Desnica, M. Ivanda, N. Radić, and P. Dubček
Ruđer Bošković Institute, 10000 Zagreb, Croatia

G. Dražić
Jožef Stefan Institute, 1000 Ljubljana, Slovenia

K. Salamon
Institute of Physics, 10000 Zagreb, Croatia

S. Bernstorff
Sincrotrone Trieste, 34102 Basovizza, Italy

V. Holý
Faculty of Mathematics and Physics, Charles University in Prague, 12116 Prague, Czech Republic
(Received 24 July 2008; revised manuscript received 7 November 2008; published 13 January 2009)

Quantum dots ordered in regular lattices, called quantum-dot superlattices, offer numerous possibilities for the creation of novel materials. The formation of such structures during multilayer deposition has been studied and explained satisfactorily only in crystalline materials. Here we are reporting the spontaneous formation of quantum-dot superlattices in amorphous systems. The observed superlattices comprise Ge quantum dots embedded in amorphous SiO_2 matrix. The internal structure and shape of Ge quantum dots can be controlled by postdeposition thermal annealing. The superlattices show collective behavior properties that appear to be the consequence of a regular ordering of quantum dots. The observed self-organized growth is explained and successfully simulated by a theoretical model based on the interplay of diffusion-mediated nucleation and surface morphology effects. The presented results can be applied more generally and show the ability of formation of regularly ordered, densely packed, and uniformly sized quantum-dot arrays in amorphous matrices.

DOI: 10.1103/PhysRevB.79.035310 PACS number(s): 81.07.Ta, 81.07.Bc, 68.65.−k, 61.46.Df

I. INTRODUCTION

Quantum-dot (QD) superlattices[1–5] hold great potential for designing new materials[6–9] through the combination of numerous geometrical arrangements[4,5] and size-dependent electrical and optical properties of QDs caused by quantum confinement effects.[10,11] The applications of semiconductor QD superlattices are promising in various fields including electronics,[7–13] quantum and nonlinear optics,[14,15] and quantum computing.[16] The Ge QDs embedded in the SiO_2 matrix are particularly interesting due to their strongly size-tunable electronic properties,[11,12,17] strong photo- and electroluminescence,[18–21] large optical nonlinearity,[22] and unusual melting or freezing conditions.[23] Such materials are also ideal for nonvolatile high-speed memory applications, due to their capacity to accept charge and hold it stable for a long time.[24,25]

The formation of semiconductor three-dimensional (3D) QD superlattices has perhaps been most frequently observed during the growth of multilayered structures,[1–5] but always in crystalline matrices. Multilayers in such systems are grown mainly by Stranski-Krastanow heteroepitaxial growth mode,[26–28] where thin crystalline layers of a semiconductor material are grown on a crystalline substrate. The main driving force for the self-organization in those systems is the misfit of the lattice constants of the growing layer and the layer below it. The misfit causes strain fields in the growing layer, which leads to the self-organized growth. However, this mechanism cannot be effective in amorphous multilayers. In amorphous systems layers containing QDs have been reported,[29–32] but without correlations in QDs positions between different layers, i.e., without 3D QD superlattice formation. Only a couple of papers[33,34] report a certain tendency toward 3D regular ordering of metallic QDs in amorphous matrices, but without a detailed explanation of the observed phenomena.

In this paper, we demonstrate the spontaneous self-organized growth of 3D semiconductor QD superlattices within completely amorphous multilayers deposited on a flat substrate and present a growth model explaining the ordering mechanism. The structure of the multilayers as well as the crystal structure of individual QDs were investigated by grazing-incidence small-angle x-ray scattering (GISAXS), high-resolution transmission electron microscopy (HRTEM), scanning transmission electron microscopy (STEM), and selected-area electron diffraction (SAED). For the characterization of the dots we used also Raman scattering. The paper is organized as follows. In Sec. II we summarize the growth procedure of the QD multilayers and show the results of TEM and GISAXS studies. Section III represents the main part of the paper; here we develop a structure model of the QD multilayer and simulate the GISAXS data; from the fit to

the experimental data we determined the parameters of the multilayer. In Sec. IV we formulate a growth model explaining the ordering mechanism and present results of a Monte Carlo simulation of the QD growth and in Sec. V we present the results of optical investigations of the dot multilayers.

II. GROWTH AND STRUCTURE OF QUANTUM-DOT MULTILAYERS

The multilayer films are grown by magnetron-sputtering codeposition of 20 alternating $(Ge+SiO_2)/SiO_2$ layers on Si(111) substrate. For the growth we used a multisource magnetron sputtering KJLC CMS-18 system; the molar ratio of $Ge:SiO_2$ was 40:60 in the mixed layers. The base pressure in the process chamber was in the range $10^{-6}-10^{-5}$ Pa, and increased several times upon the cryopump throttling; the working gas was 5.5 N argon at 0.5 Pa pressure. Pure (Ge) and pure SiO_2 (99.995%) were used as targets in the dc (14 W) and rf (250 W) operated magnetrons, respectively. The deposition rates were 2.2 nm/min for the Ge target and 6.7 nm/min for the SiO_2 target. The thickness ratio in a unit bilayer was controlled by the shutter operation in the respective magnetrons, and the thickness of each layer being about 7 nm. A (111) silicon substrate was mounted onto the substrate holder which rotated (10 rpm) during the codeposition in order to achieve lateral homogeneity of the $Ge+SiO_2$ mixture. The deposition was performed onto substrates held at 500 °C.

After the deposition, the samples were annealed at different temperatures up to 900 °C. The substrate Si(111) surface is chosen since two-dimensional (2D) diffusion of the adatoms at a (111) Si surface is more isotropic than on (001), for instance, where ⟨110⟩ dimmers affect the diffusion anisotropy. We have also used the amorphous SiO_2 substrates, and practically the same results have been obtained.

Transmission electron microscopy images have been taken at the JEOL2010F microscope, operated at 200 kV and equipped with a field-emission gun and a high-angle annular dark-field detector (HAADF) for Z-contrast imaging. The images of the as-deposited (AS) film and of the films annealed at different temperatures (T_a=700 and 800 °C) shown in Figs. 1(a)–1(f) and 4(a) exhibit several important structural properties:

(i) The deposited films consist of well-defined layers containing QDs [Figs. 1(a)–1(c)]. The layered structure is stable for annealing temperatures up to 900 °C [Fig. 4(a)].

(ii) HRTEM analysis indicates that QDs are already formed during the deposition process [see the inset in Fig. 1(a)]. The shape and the internal structure of the formed QDs depend on the annealing temperature [insets of Figs. 1(a)–1(c)]: QDs in the AS film consist of amorphous Ge, with elongated, irregularly shaped QDs, tilted in respect to the sample surface; for T_a=700 °C the crystallization of the QDs starts, so the amorphous and crystalline Ge phases are found in the same QD. The shape of QDs for this annealing temperature is similar to the QDs shape in the AS film. The annealing at T_a=800 °C causes a complete crystallization of germanium constituting the QDs, and transformation of QDs shape from elongated (obtained during the deposition) to spherical. The selected area electron diffraction (SAED) pattern analysis presented in Fig. 2 shows that formed QDs consist of crystalline Ge, with the diamond unit cell belonging to the space group $Fd\bar{3}m$ as in Ge bulk. The SAED analysis also reveals a low level of imperfections, i.e., good crystalline quality of the formed QDs.

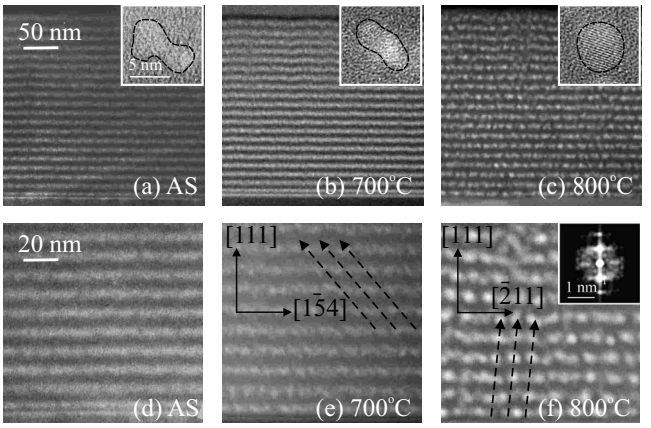

FIG. 1. Cross-section STEM pictures of the QD multilayers with smaller [panels (a), (b), and (c)] and larger magnification [(d), (e), and (f)]. The annealing temperatures are indicated. The insets in the upper-row panels show individual dots depicted by HRTEM; the inset in panel (f) contains the 2D Fourier transformation of the STEM image demonstrating the ordering of the dot positions. The dashed arrows indicate the direction of the correlation of the dot positions at subsequent interfaces; the Miller indices are defined to the averaged dot lattice with the lattice vectors $\langle \boldsymbol{a}_{1,2,3} \rangle$.

(iii) The most interesting property is domains indicating regularly ordered QDs, visible in STEM cross sections in Figs. 1(a)–1(f). The FCC-like *ABCABC* QDs stacking indicates their arrangement in 3D rhombohedral ($R\bar{3}m$) lattice with the [111] axis perpendicular to the sample surface. Thus, within a domain, each layer of the superlattice consists of hexagonally ordered QDs, while the layers have an *ABCABC* stacking sequence.

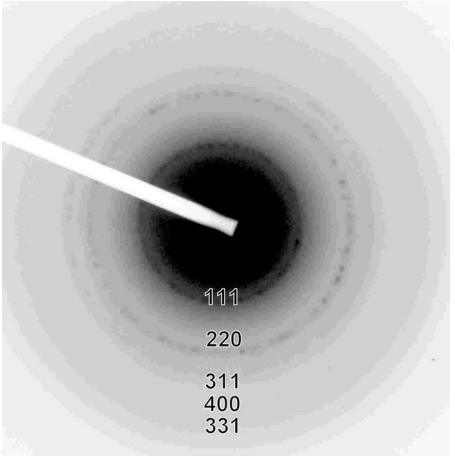

FIG. 2. Selected area electron diffraction of the T_a=800 °C film. The observed reflections show formation of Ge nanocrystals with the diamond unit cell belonging to the space group $Fd\bar{3}m$ as in Ge bulk.

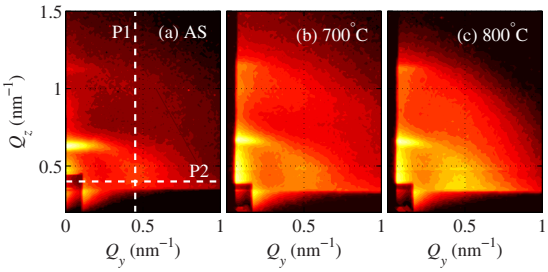

FIG. 3. (Color online) GISAXS two-dimensional reciprocal-space maps of samples AS, T_a=700 °C and T_a=800 °C. The lines P1 and P2 in panel (a) denote the trajectories of linear scans, depicted in Fig. 6. The step of the intensity contours is $10^{0.2}$.

The STEM images show cross sections of the films in real space from a relatively small part of the sample, so we apply a GISAXS analysis,[28,35,36] which provides structural data in reciprocal space with excellent statistics (approximately 10^{12} QDs in the irradiated sample volume). The GISAXS measurements have been performed at the synchrotron Elettra, Trieste with photon wavelength 0.154 nm, and several incidence angles above the critical angle of total external reflection. The scattered x-ray intensity has been measured by a 2D x-ray detector; its entrance window was perpendicular to the sample surface and to the plane of incidence of the primary radiation. The measured 2D intensity distributions were transformed to reciprocal space, so that 2D reciprocal-space maps in Q_yQ_z plane perpendicular to the sample surface and to the plane of incidence were obtained.

In the reciprocal-space maps depicted in Figs. 3(a)–3(c) the regular ordering of QDs causes appearing of intense diffraction (Bragg) spots. The spot arrangement is the same for all films and is in accordance with the formation of 3D QD superlattices, with rhombohedral structure and certain degree of disorder, just as was found by STEM. The superlattices appear in domains that are randomly rotated around the surface normal. In the case of the T_a=900 °C sample, the QDs are completely disordered so that no Bragg spots are visible in the GISAXS intensity map [Fig. 4(b)].

III. ANALYSIS OF THE X-RAY SCATTERING RESULTS

We have developed a structure model of a QD superlattice enabling us to simulate the GISAXS intensity and to determine parameters for a quantitative characterization of the degree of the dot ordering. This structure model is purely phenomenological and it is based on the well-known paracrystal structure model.[37] In Sec. IV we present a simple Monte Carlo simulation of the dot growth based on the paracrystal model.

For the simulation of x-ray scattering the distorted-wave Born approximation (DWBA) is used,[4,28] in which the scattering sample is divided into two parts—the nondisturbed system (a semi-infinite amorphous substrate, in our case), and the disturbance (the dots). Then, the intensity diffusely scattered into a given point $\boldsymbol{Q}$ in reciprocal space can be expressed as

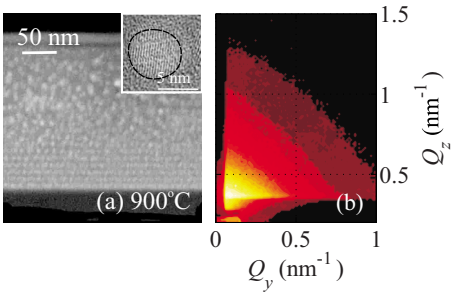

FIG. 4. (Color online) (a) STEM image, the corresponding HR-TEM image of typical QD (inset), and (b) the GISAXS intensity map of the film annealed at T_a=900 °C. After the annealing, disintegration of the layered structure is evident in the upper part of the STEM image. The GISAXS map shows no Bragg peaks so that the QDs are not regularly ordered.

$$I(\boldsymbol{Q}) = A|t_i t_f|^2 \left\langle \left| \sum_j F_j(\boldsymbol{Q}_T) e^{-i\boldsymbol{Q}_T \cdot \boldsymbol{R}_j} \right|^2 \right\rangle. \quad (1)$$

Here A is a constant containing the intensity of primary beam, the integral acceptance of the detector, the contrast in the polarizabilities of the inclusion and the host material, among others. $t_{i,f}$ are the Fresnel transmission coefficients of the free surface for the primary and scattered beams, respectively; the term $|t_i t_f|^2$ gives rise to the Yoneda peak in the points in reciprocal space, in which the incidence and/or exit angles equal the critical angle of total external reflection. $\boldsymbol{Q}_T$ is the complex scattering vector corrected to refraction, F_j is the structure factor of the jth dot, its center is in point $\boldsymbol{R}_j$. The averaging $\langle\ \rangle$ is performed over a statistical ensemble of all positions and sizes of the inclusions.

The coordinates $Q_{x,y,z}$ can be calculated from the given incidence angle α_i and position $(y_D z_D)$ of a pixel on the 2D detector. We assume that the detector plane is (yz), the plane of incidence is (xz), and the horizontal distance sample detector is L. Simple geometrical considerations yield the following formulas for the exit angle α_f and for the in-plane scattering angle θ:

$$\theta = \arctan(y_D/L), \quad \alpha_f = \arctan(z_D/\sqrt{L^2 + y_D^2}). \quad (2)$$

Then, the coordinates of the scattering vector are

$$Q_x = K(\cos\ \alpha_f \cos\ \theta - \cos\ \alpha_i),$$

$$Q_y = K \cos\ \alpha_f \sin\ \theta, \quad Q_z = K(\sin\ \alpha_f + \sin\ \alpha_i), \quad K = 2\pi/\lambda. \quad (3)$$

The in-plane components $Q_{Tx,Ty}$ of the refracted scattering vector are not affected by refraction, i.e., $Q_{Tx,Ty}=Q_{x,y}$, the vertical component is

$$Q_{Tz} = K(\sqrt{\sin\ \alpha_f^2 - 2\delta} + \sqrt{\sin\ \alpha_i^2 - 2\delta}),$$

where $\delta=1-n$. n is the complex refraction index of the nondisturbed system.

The structure factor of a dot is the Fourier transformation of its shape function (unity in the dot volume, zero outside it). We assume that the dots have the shape of a uniaxial ellipsoid (spheroid) with the lateral and vertical radii R_{LV}, respectively. The structure factor is

$$F(\boldsymbol{Q}) = 4\pi R_L^2 R_V \frac{\sin\kappa - \kappa\cos\kappa}{\kappa^3}, \quad \kappa = \sqrt{R_L^2 Q_L^2 + R_V^2 Q_V^2}. \tag{4}$$

Here $Q_{L,V}$ are the components of $\boldsymbol{Q}$ parallel to $R_{L,V}$, respectively.

In the following we assume that the size of the dot is not statistically correlated with its position. The expression in Eq. (1) can therefore be simplified writing[38]

$$I(\boldsymbol{Q}) = A|t_i t_f|^2\{[\langle|F(\boldsymbol{Q}_T)|^2\rangle - |\langle F(\boldsymbol{Q}_T)\rangle|^2]G_\perp(Q_{Tz}) + |\langle F(\boldsymbol{Q}_T)\rangle|^2 G(\boldsymbol{Q}_T)\}, \tag{5}$$

where

$$G_\perp(Q_{Tz}) = \frac{e^{-2NT\,\mathrm{Im}(Q_{Tz})} - 1}{e^{-2T\,\mathrm{Im}(Q_{Tz})} - 1},$$

N is the number of the $(\mathrm{Ge}+\mathrm{SiO_2})/\mathrm{SiO_2}$ bilayers, and

$$G(\mathbf{Q}_T) = \left\langle \sum_{j,k} e^{-i(\boldsymbol{Q}_T\cdot\boldsymbol{R}_j - \boldsymbol{Q}_T^*\cdot\boldsymbol{R}_k)} \right\rangle \tag{6}$$

is the correlation function of the dot positions. The averaging of the structure factor F and of its square is performed over the sizes of the dots and the orientations of their rotation axis. In the last formula, R_j is the position vector of the dot j and the averaging is carried out over random dot positions.

For the evaluation of the correlation function we have used a modification of the paracrystal model,[37] assuming that the z-coordinate Z_j of the dots at the jth interface (perpendicular to the sample surface) is not random: $Z_j = jT$, where T is the superlattice period. The basic assumption of a one-dimensional (1D) paracrystal model is that the distances between neighboring dots are random with a given mean and dispersion; the distances $L_j = X_j - X_{j-1}$ and $L_{j+1} = X_{j+1} - X_j$ are statistically independent. We have assumed that the lateral dot positions at the substrate surface (zeroth interface) obey a 2D paracrystal model, and the correlation of the lateral positions of the dots at different interfaces follows from a 1D paracrystal model. Instead of using the dot distances, we introduce random vectors $\boldsymbol{a}_{1,2,3}$ of a 3D dot lattice. We choose the vectors $\boldsymbol{a}_{1,2}$ parallel to the sample surface and $\boldsymbol{a}_{3z} = T$ (see Fig. 5). The averaged vectors $\langle\boldsymbol{a}_{1,2,3}\rangle$ define the ideal rhombohedral lattice of the dots. In the following, the index j of the dot considered as a vector (j_1, j_2, j_3), its component j_p refers to the component of the dot position vector along $\boldsymbol{a}_p$.

Using the assumptions above, we obtain the correlation function in the form

$$G(\mathbf{Q}_T) = G_\parallel(\boldsymbol{Q}_\parallel)\{G_\perp(Q_{Tz}) + 2\,\mathrm{Re}[G_{\parallel\perp}(\boldsymbol{Q}_T)]\}, \tag{7}$$

where

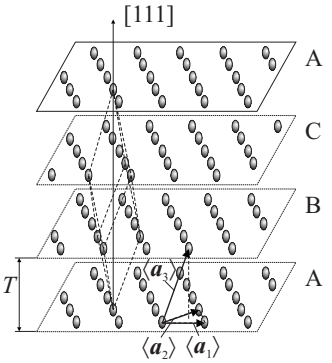

FIG. 5. Schematic sketch of the rhombohedral ordering of the quantum dots, expressed as am *ABCABC* sequence of 2D hexagonal dot arrays. $\langle\boldsymbol{a}_{1,2,3}\rangle$ are the basis vectors of the averaged dot lattice; the [111] direction in the lattice is perpendicular to the sample surface.

$$G_\parallel(\boldsymbol{Q}_\parallel) = \left\langle \sum_{j,k;j_3=k_3=0} e^{-i\boldsymbol{Q}_\parallel\cdot(\boldsymbol{X}_j - \boldsymbol{X}_k)} \right\rangle$$

is the correlation function of the lateral positions of the dots at the zeroth (substrate) interface, and the term $G_{\parallel\perp}$ expresses the correlation of the lateral positions of the dots lying at different interfaces.

If we use a 2D paracrystal model for the description of the dot positions at the substrate interface, we obtain

$$G_\parallel(\boldsymbol{Q}_\parallel) = M^2 \prod_{p=1,2} \left[1 + 2\,\mathrm{Re}\left(\frac{\xi_p}{1-\xi_p}\right)\right]. \tag{8}$$

Here M^2 denotes the number of the dots at the substrate surface ($M \gg 1$ is assumed). The 1D paracrystal model for the correlation of lateral positions of the dots at different interfaces yields

$$G_{\parallel\perp}(\boldsymbol{Q}_T) = \frac{1}{\psi^* - 1}\left(\frac{|\psi|^{2N} - |\psi|^2}{|\psi|^2 - 1} - \frac{\psi^N - 1}{\psi - 1}\right). \tag{9}$$

We have denoted $\psi = \xi_3 e^{-iQ_{Tz}T}$ and $\xi_p = \langle e^{-i\boldsymbol{Q}_\parallel\cdot\boldsymbol{a}_p}\rangle$, $p = 1,2,3$. Assuming normal distribution of the dot distances, we obtain

$$\xi_{1,2} = e^{-i\langle\boldsymbol{a}_{1,2}\rangle\cdot\boldsymbol{Q}_\parallel} e^{-\sigma_{\parallel\parallel}^2|\mathbf{Q}_\parallel|^2/2}, \quad \xi_3 = e^{-i\langle\boldsymbol{a}_3\rangle\cdot\boldsymbol{Q}_\parallel} e^{-\sigma_{\parallel\perp}^2|\mathbf{Q}_\parallel|^2/2},$$

where $\sigma_{\parallel\parallel}$ and $\sigma_{\parallel\perp}$ are the root-mean-square (rms) dispersions characterizing the lateral and vertical correlations of the lateral dot positions, respectively.

Summarizing this part, the structure model of the 3D dot lattice is characterized by the following parameters: the average lattice vectors $\langle\boldsymbol{a}_{1,2,3}\rangle$ and the rms dispersions $\sigma_{\parallel\parallel}$, $\sigma_{\parallel\perp}$, the shape of the dot is defined by the radii $R_{L,V}$, the rms dispersion σ_R of the dot sizes and by the angle of the rotation axis of the dot ellipsoid with the z axis.

The distribution of the values $G(\boldsymbol{Q})$ of the correlation function in reciprocal space exhibits a sequence of Bragg-type peaks in the points of the lattice reciprocal to the averaged dot lattice with the lattice vectors $\langle\boldsymbol{a}_{1,2,3}\rangle$. The rms dispersions $\sigma_{\parallel\parallel}$, $\sigma_{\parallel\perp}$ can be determined from the dependence of the lateral and vertical widths $\Delta Q_\parallel$, ΔQ_z of these satellites on $|\boldsymbol{Q}_\parallel|$. From the paracrystal model it follows that

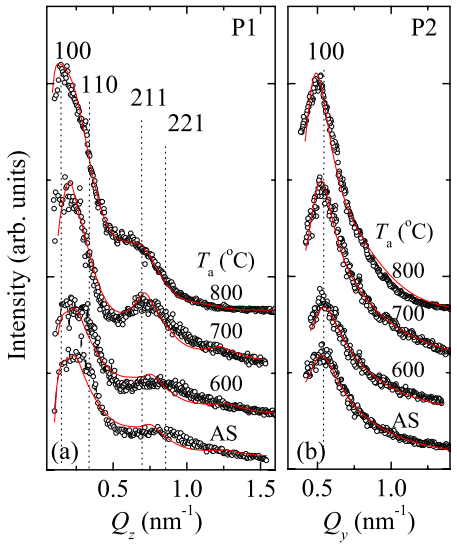

FIG. 6. (Color online) The linear scans extracted from the experimental 2D GISAXS reciprocal-space maps shown in Fig. 2 along the lines (a) P1 and (b) P2—points, and their fits (lines). The annealing temperatures T_a are indicated. The vertical lines along with the corresponding Miller indices denote the theoretical positions of the points of the lattice reciprocal to the averaged dot lattice.

$$\Delta Q_{\parallel} \approx \frac{1}{2}\sigma_{\parallel\parallel}|\boldsymbol{Q}_{\parallel}|^2, \quad \Delta Q_{\perp} \approx \frac{1}{2}\sigma_{\parallel\perp}|\boldsymbol{Q}_{\parallel}|^2,$$

if N, $M \gg 1$. In the simulation of the GISAXS reciprocal-space maps we have assumed that the rhombohedral lattice of QDs consists of domains ("grains") randomly rotated around the surface normal. Then NM^2 denotes the number of the dots in one domain. The waves scattered by individual domains have random phases so that the total scattered intensity is a sum of intensities emitted by individual grains. We believe that there is no physical reason for a long-range order spontaneous arrangement of the dots through the whole film volume since the dot positions are influenced only by neighboring dots in the lateral direction and by the positions of the dots at two interfaces, preceding the actually growing interface. A long-range order arrangement of the dots would require predefined ideally periodic positions of the dots (preferred positions) through the whole film, from which the actual positions would randomly deviate.

TABLE I. Structural parameters of the QD multilayers determined from the GISAXS data.

T_a (°C)	AS	600	700	800
$\langle\lvert\boldsymbol{a}_{1,2}\rvert\rangle$ (nm)	11.6 ± 0.9	12.0 ± 0.8	12.3 ± 0.8	12.3 ± 0.4
$\langle a_{3z}\rangle \equiv T$ (nm)	12.3 ± 0.3	12.3 ± 0.3	12.3 ± 0.3	12.3 ± 0.3
$\sigma_{\parallel\parallel}$ (nm)	3.5 ± 0.8	3.5 ± 0.5	3.5 ± 0.4	3.6 ± 0.2
$\sigma_{\parallel\perp}$ (nm)	2.1 ± 0.8	2.3 ± 0.5	2.3 ± 0.5	3.3 ± 0.2
R_L (nm)	1.2 ± 0.4	1.2 ± 0.2	1.2 ± 0.1	2.7 ± 0.1
R_V (nm)	1.7 ± 0.6	2.6 ± 0.5	3.2 ± 0.2	2.7 ± 0.1
σ_R (nm)	0.5 ± 0.2	0.5 ± 0.2	0.4 ± 0.1	0.4 ± 0.5

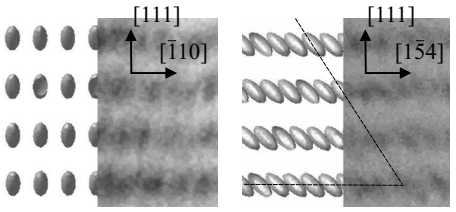

FIG. 7. Elongation of QDs in [$\bar{3}$11] direction, found for the $T_a < 800$ °C films: the simulations and the corresponding experimentally obtained STEM images of the QD superlattice cross sections obtained for $T_a = 700$ °C. The samples' orientations are indicated in the figure; the simulation parameters are taken from the results of GISAXS analysis.

In order to determine the structure parameters listed above, we have fitted two vertical and two horizontal linear scans extracted from the measured 2D intensity maps (see Fig. 3). The experimental and fitted linear scans are depicted in Fig. 6, the resulting structural parameters are summarized in Table I. From the very good fit of the measured and simulated scan it follows that the model used well reproduces the actual dot distribution. The QDs arrangement can be well described by means of the rhombohedral lattice (see Fig. 5) with a relatively low disorder level. The standard deviation of neighboring in-plain QDs distances is found to be lower than 27% of the distance value in ideal lattice. The shape of QDs is found tunable by the annealing temperature: for the AS and the $T_a < 800$ °C films, QDs are elongated and tilted in respect to the substrate surface, while for $T_a = 800$ °C QDs are spherical, all in keeping with the HRTEM and STEM findings. All of the films have a narrow QDs size distribution and the high density (approximately 6×10^{17} QDs/cm^3). Interestingly, the elongation of QDs preferentially occurs in the same crystallographic direction $\langle\bar{3}11\rangle$ of the formed QD superlattice. In that direction the neighboring QDs centers are maximally separated. When those findings are built into the 3D simulation of the observed superlattice ($T_a = 700$ °C), an excellent agreement with the STEM observations in Fig. 1 is obtained again. This fact is demonstrated in Fig. 7, where we compare the STEM pictures of individual QDs in sample $T_a = 700$ °C with the shapes of the dots reconstructed from

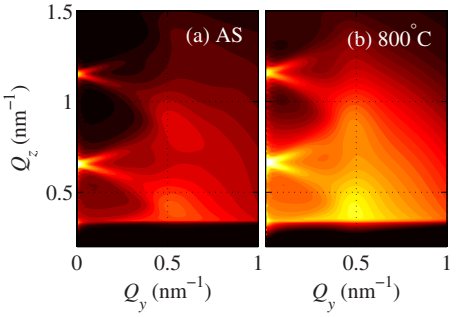

FIG. 8. (Color online) The simulated GISAXS reciprocal-space maps of samples AS and $T_a = 800$ °C, using the structure parameters obtained from the fit of the line scans (see Table I). The step of the intensity contours is $10^{0.2}$.

the parameters obtained from the fitting of the GISAXS data. As follows both from STEM and from GISAXS methods, the QDs are elongated indeed in the $[\bar{3}11]$ direction.

Figures 8(a) and 8(b) contain the simulated GISAXS intensity maps of samples AS and T_a=800 °C using the parameters in Table I. From the comparison with the measured GISAXS maps in Fig. 3 it follows again that the structure model of the dot ordering well describes the positions of the QDs in our samples.

IV. MONTE CARLO SIMULATION OF THE SELF-ORGANIZATION OF THE DOTS

The basic principles of the observed self-organized growth and rhombohedral QDs arrangement are underpinned by a simple growth model. The model is constructed as a combination of two mechanisms: (i) diffusion-mediated nucleation[39–41] and (ii) enhanced nucleation probability in the troughs of the underlying substrate.[42,43] Each of these two mechanisms has been separately experimentally verified.[39–43] Here we show that their combination under certain experimental conditions can indeed create 3D ordering.

The first mechanism assumes that nucleation of QDs is mediated by diffusion properties of atoms coming to the surface during the deposition process.[39–41] The consequence of this mechanism is the formation of QDs which are to some degree spatially correlated. The surface diffusion is stimulated by the elevated substrate temperature (500 °C in our case). The nucleation of a QD starts when the concentration of diffusing Ge atoms reaches the critical value at some surface point.[39] Thus formed nuclei become less mobile and grow by capturing of nearby diffusing Ge atoms. Consequently, the concentration of Ge atoms is lowered in the region close to every formed nucleus, thus preventing another nucleation in that region. Due to this process, QDs distances are correlated.[19,39,40] We have described the correlation of QDs distances by disordered hexagonal lattice with the mean basis vectors $\langle \boldsymbol{a}_{1,2} \rangle$ introduced earlier. The type of disorder[37,44] (deviations from the ideal lattice) is quantified by the statistics of the random shift vectors $\boldsymbol{\varphi}$ describing the displacement of QDs from their positions in the ideal hexagonal lattice according to Fig. 9(a), and expressed numerically by the rms deviation $\sigma_{\parallel\parallel} = \sqrt{|\boldsymbol{\varphi}|^2}$. The hexagonal lattice is chosen since surfaces and surface diffusion properties are isotropic in the plane where the nucleation occurs.[40] The first mechanism itself results in the structure consisting of QDs spatially correlated within each layer, but with no interlayer correlations.

The second mechanism, based on surface morphology effects, supposes that the nucleation probability is enhanced in the regions with negative curvature (troughs) on the surface [Fig. 9(b)]. This leads to the interlayer correlations of the QD positions. This mechanism has been experimentally proven to work in Ge nucleation on prepatterned amorphous SiO_2 surfaces[42,43] and is explained as surface potential minimization.[42] Our STEM analysis shows that hills indeed occur above every formed QD, while the troughs occur between them [see the inset in Fig. 9(b)]. Thus, after the deposition of the first bilayer, the surface layer contains the troughs which act as preferential nucleation sites for the QDs in the next layer. In that way, QD geometry of the first layer influences the geometry of all subsequent layers. This mechanism is crucial for reaching the self-ordered growth, and it can reduce the degree of QD spatial disorder in each subsequent layer.

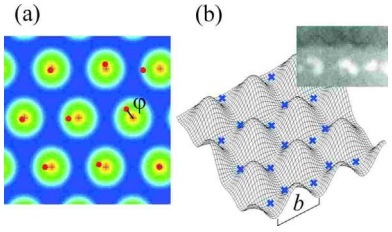

FIG. 9. (Color online) Illustration of the growth model and simulation of the observed self-organized growth. Panel (a): the positions of QDs (circles) in a layer. Random vectors $\boldsymbol{\varphi}$ express the positions of QDs as displacement from the sites of an ideal hexagonal lattice (crosses). (b) Possible QDs nucleation sites (crosses) lay within the troughs of the underlying surface. The inset shows the cross-sectional STEM image of the AS sample surface, where the hills are visible above each QD while the troughs occur between them. The width of the hills in the simulation is assumed to be Gaussian-type, with the standard deviation b.

In 3D systems, generally there are more troughs at the surface than the QDs in the layer underneath. Thus, if only the second mechanism was functional, then the number of QDs would increase in every new layer and the QD size would be reduced. However, the diffusion dynamics, i.e., the first mechanism, demands the same nature of diffusion and the same nucleation properties in all layers and keeps QD sizes and their number practically constant in each layer. The nucleation therefore will occur only in those minima which are in accordance with the requirements of the diffusion mechanism. Furthermore, all already deposited layers influence the surface morphology of the current top layer, inducing *ABCABC* layer stacking (see also Fig. 5).

Considering two mechanisms mentioned above, we have developed a simple kinetic Monte Carlo algorithm, simulating the nucleation and growth of quantum dots in a multilayer. The algorithm consists of the following steps:

(1) Define the positions of the dots for the starting layer. The positions are given by a disordered 2D hexagonal lattice. The disorder type is chosen to be a combination of an ideal paracrystal and uncorrelated disorder.[37,45] For the uncorrelated disorder the position of the jth dot $[j \equiv (j_1, j_2, 0)]$ is given by

$$\boldsymbol{X}_{j_1,j_2} = j_1 \langle \boldsymbol{a}_1 \rangle + j_2 \langle \boldsymbol{a}_2 \rangle + \boldsymbol{\varphi}_{j_1,j_2}, \tag{10}$$

where $\boldsymbol{\varphi}_{j_1,j_2}$ is in-plain random shift (see Fig. 9). The paracrystal component of the disorder is given by a pair of random vectors $\boldsymbol{\delta}^{(1,2)}_{j_1,j_2}$ defined as

$$\boldsymbol{X}_{j_1,j_2} = \boldsymbol{X}_{j_1-1,j_2} + \langle \boldsymbol{a}_1 \rangle + \boldsymbol{\delta}^{(1)}_{j_1,j_2} = \boldsymbol{X}_{j_1,j_2-1} + \langle \boldsymbol{a}_2 \rangle + \boldsymbol{\delta}^{(2)}_{j_1,j_2}. \tag{11}$$

The statistics of the shift vectors $\boldsymbol{\varphi}$ and $\boldsymbol{\delta}^{(1,2)}$ determines the disorder properties. Thus, for every site of ideal hexagonal

lattice, one position of QD is chosen in accordance with the given disorder properties. Standard deviation of QD distances is $\sigma_{||||}$.

(2) Suppose that hills exist above each formed QD after the deposition of the spacer SiO_2 layer. For the shape of the hills at the interface j_3 we assumed 2D Gaussian-type functions given by

$$h_{j_3}(\boldsymbol{x}) = \sum_{j_1,j_2} [f(\boldsymbol{x} - \boldsymbol{X}_{j_1,j_2,j_3-1}) + Cf(\boldsymbol{x} - \boldsymbol{X}_{j_1,j_2,j_3-2})],$$

$$f(\boldsymbol{x}) = \exp(-|\boldsymbol{x}|^2/b^2), \tag{12}$$

where b is a suitably chosen parameter determining the width of the hills. The shape function $h_{j_3}(\boldsymbol{x})$ of the current layer comprises the hills above the QDs in the previous layer j_3-1 (in the positions $\boldsymbol{X}_{j_1,j_2,j_3-1}$) and above the QDs in layer j_3-2 ($\boldsymbol{X}_{j_1,j_2,j_3-2}$), the heights of the latter are reduced by the "inheritance factor" $C<1$). If we choose $C=0$, the QDs in the layer j_3 will be affected only by the QDs in the layer j_3-1, which will lead to both *ABCABC* and *ABAB* stackings with the same probability. Since, as we showed experimentally, the *ABCABC* stacking is always preferred, the second term in the expression for $h_{j_3}(\boldsymbol{x})$ must be included.

(3) Find the minima of the resulting surface. The found minima are potential nucleation sites for the next layer.

(4) For every site of ideal hexagonal lattice choose the minimum (i.e., the nucleation site) which best satisfies the initially given disorder property. If there is no such minimum, then choose the nucleation site by the procedure described in step 1.

(5) Place the QDs in the centers of mass of the Voronoi cells (part of the surface closer to given minimum than to any other)[41] corresponding to nucleation sites. This step is introduced to take into account the effect of unequally spaced nucleation places (minima) which then capture more (or less) Ge atoms at the side where neighboring nuclei are more (or less) distanced. It is equivalent to a uniform deposition of Ge atoms on the surface and diffusion of them to the nearest minima chosen by step 4.

(6) Repeat the procedure described in steps 2–5.

Examples of the simulation results are depicted in Figs. 10 and 11. In these figures we have indicated the generated dot positions in the zeroth substrate interface, and in the interfaces 3 and 5, the simulated cross section of the QD multilayer, as well as the histogram of the dot sizes in the whole simulated multilayer stack. The volume of each QD (circles) is proportional to the area of corresponding Voronoi cell (lines). Cross sectional view of the first 12 layers shows the existence of vertical correlation of the QDs distances with the *ABCABC* layer stacking.

Figures 10 and 11 demonstrate the influence of the parameter C on the resulting dot multilayer. In both figures we have used the values $\sigma_{||||}=2.3$ nm and $b=4$ nm; the simulations differ in the value of the "inheritance factor" C. If we put $C=0.75$, i.e., if the QD positions in the layers j_3-2 and j_3-1 have almost the same influence on the surface morphology of the layer j_3, we obtained a slightly disordered rhombohedral dot lattice, with the rms dispersion of the distribution of the dot sizes of about 1 nm (see Fig. 10). In this figure, the disorder degree is decreasing in the first several layers with the number of deposited layers. In the layers above them, the disorder is increasing due to the strong influence of the morphology of the layers below. The same is observed in the experimentally measured STEM cross sections [Figs. 1(c) and 1(f)].

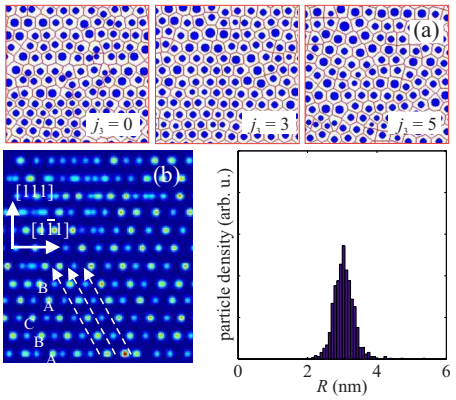

FIG. 10. (Color online) Results of the Monte Carlo simulations of the dot growth. (a) Positions and sizes of the dots on the substrate surface $j_3=0$, and on the interfaces $j_3=3,5$. The diameter of the circles represents the size of a particular dot; the lines denote the Voronoi polygons, from which the adatoms are attracted to a growing dot. (b) Simulated cross section of a QD multilayer; the growth direction corresponds to the [111] direction in the dot lattice. The *ABCABC* stacking is indicated. (c) Histogram of the dot sizes in the multilayer. In the simulation, the inheritance factor $C=0.75$ was assumed.

If we choose $C=0.25$, the dot ordering substantially improves and the distribution of the dot sizes becomes narrower (rms dispersion of about 0.5 nm, Fig. 11). Then, the in-layer disorder is decreasing, and the QDs sizes are unifying with the number of deposited layers trough the whole film thickness. Such regime can be achieved by choosing the optimal growth parameters, including the initial disorder lower than $\approx 0.25a$, ($a=|\langle \boldsymbol{a}_{1,2}\rangle|$ is the QDs neighboring distance in an ideal hexagonal lattice); some, but not too high influence of the layers below morphology ($C \approx .0.25$) and present surface morphology features ($b \approx 0.6a$). If we use $C=0$, the dot lat-

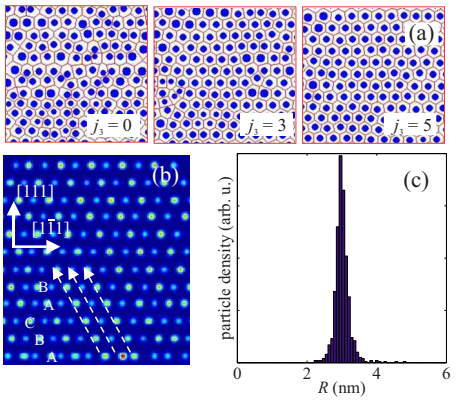

FIG. 11. (Color online) The same situation as in Fig. 10, $C=0.25$.

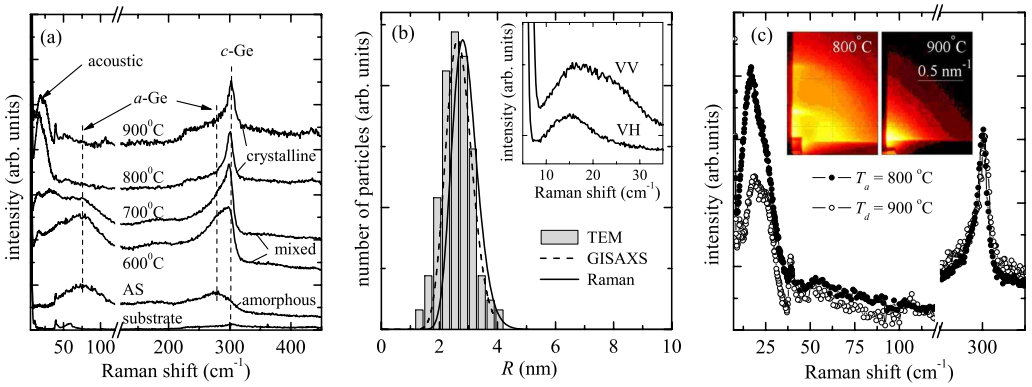

FIG. 12. (Color online) (a) Raman spectra of the as-deposited and of the annealed films. (b) Size distribution of the QDs calculated from the acoustic vibrational modes for the T_a=800 °C film. The insets show polarized (VV) and depolarized (VH) low-frequency Raman spectra from which the size distribution is calculated. (c) The comparison of the relative intensities of depolarized spectra obtained on the film with QDs ordered in the QD superlattice (annealing T_a=800 °C), and on the films where ordering is not found (T_a=900 °C). The spectra are normalized to the Ge transversal optical mode at 300 cm^{-1}, i.e., to the same volume of the Raman excited samples. In the insets we show the corresponding GISAXS maps for comparison.

tice becomes completely disordered since both *ABCABC* and *ABAB* stacking types may occur simultaneously.

From the Monte Carlo simulations of the growth it follows than the partly or fully deterministic growth comprises preferentially regular QDs ordering and formation of QD superlattices with rhombohedral structure, whose size distribution and degree of disorder are dependent on the deposition parameters. This regime can be achieved if the QDs are formed already during the deposition process, if the surface morphology of each layer follows the morphology of the QDs in it, and if the lateral disorder induced by diffusion properties described by $\sigma_{||||}$ is not too high. Furthermore, the surface morphology of the growing layer should "feel" the influence of the layers underneath; insuring the *ABCABC*-like stacking of layers, which is accomplished by a suitable choice of the parameter *C*. The QD superlattices reported in this paper are well described by the partly deterministic growth type. If by fine tuning of the growth parameters a reasonably low initial disorder and moderately undulated morphology of a layer below is achieved, the model predicts the self-ordering of QDs in a perfectly ordered 3D lattice as shown in Figs. 10 and 11.

On the other hand, a nonordered QD growth occurs if any of growth conditions do not produce the above given requirements which lead to the ordered growth. For example, if the hills above each QD are very small or nonexisting after the deposition of the spacer layer, then second mechanism cannot act, and interlayer correlations will not occur. The same occurs if the lateral in-layer correlations in QD distances are very small or nonexisting (large $\sigma_{||||}$) due to the diffusion properties. Then each QD can nucleate in a relatively large region around its "ideal" position. That region contains many surface minima (possible nucleation sites) resulting in absence of vertical correlations. Thus, the achieving of the conditions for the growth of QD superlattices needs careful selection of deposition parameters. Deposition temperature and rate influence the diffusion properties which further influence the properties of QDs and surface morphologies. Proper layer thicknesses and compositions are also very important. These conditions, emerging from the model, are well supported by our experimental results on similar systems.[32]

V. OPTICAL MEASUREMENTS

The multilayer properties are further investigated by Raman spectroscopy (Fig. 12). Amorphous Ge (*a*-Ge) transversal-like optical bands are present for T_a<800 °C films, while the crystalline Ge (*c*-Ge) transversal optical (TO) line at 300 cm^{-1} is present for the all annealed films. These results confirm the HRTEM and SAED findings: Ge QDs in AS film are amorphous, in the T_a=600 °C, 700 °C films they are partially crystalline, while for $T_a \leq$800 °C, the Ge QDs are completely crystalline. There are no evidences of Ge-Si or Ge-O vibrations, what indicates that the QDs have a pure Ge composition.

The full width at half maximum (FWHM) of the TO *c*-Ge Raman line for the film annealed at 800 °C (FWHM $\approx$13.5 cm^{-1}) is much wider than the corresponding bulk Ge value (FWHM$\approx$3.7 cm^{-1}).[46] Such a broadening of the Raman line could be explained by strong quantum confinement in small Ge QDs.[46–48] In principle the homogeneous linewidth of phonon Raman lines is determined by anharmonic interactions (phonon decay). However, FWHM of the TO *c*-Ge Raman line for the film annealed at 800 °C (FWHM $\approx$13.5 cm^{-1}) is much wider than the phonon decay bulk Ge value (FWHM$\approx$3.7 cm^{-1}). The phonon confinement model should mainly contribute to the observed downshift and a broadening of the low-frequency side of the phonon line depending on the size and shape of the microcrystallines.[47,48] The experimentally measured value of the broadening of this TO Raman line is in excellent agreement with the theoretical predictions[46] for Ge QDs with the radius close to 3 nm; a size of QDs which is obtained from the STEM and from the GISAXS analysis.

Spherical acoustical vibrations[49] of formed Ge QDs produce the strong Raman bands visible at low frequencies in Fig. 12(a). These low-frequency Raman (LFR) modes are most pronounced for the T_a=800 and 900 °C samples, con-

firming the formation of well-defined spherical and crystalline Ge QDs in those samples. The theoretical description[49] enables the calculation of QD size distribution from such LFR modes [Fig. 12(b)]. The size distribution of the quantum dots has been obtained from the polarized and depolarized low-frequency Raman spectra shown in the inset in Fig. 12(b). The mean QD radius is 2.8 nm and the rms deviation of the size distribution is 0.5 nm. Agreement with the STEM and with the GISAXS results is reasonably good.

The interesting collective behavior of the formed QDs comes to light when the LFR modes measured on the samples with and without regular QD ordering are compared. For that purpose, the intensity of LFR quadrupolar vibrational mode[49–51] of the T_a=800 °C film is compared with the equivalent vibrational mode obtained on film annealed at T_a=900 °C, where the QDs are not ordered in superlattices [see Fig. 12(c); the insets demonstrate different degrees of order in the T_a=800 and 900 °C samples, and see also Fig. 4]. The obtained Raman spectra make obvious that the intensity from the ordered film is much higher than the second intensity. However, the QD compositions are very similar for both samples and do not significantly influence the differences in Raman intensities, and in addition, effects of different QD size distributions are also eliminated as possible source of the enhanced intensity.

The most plausible explanation of changes in intensity is the collective effect of quadrupolar vibrations which appear when QDs become organized in superlattices. Due to the regular arrangement, the QDs vibrate coherently resulting with the considerable increases in the intensity of the quadrupolar vibrational mode. Such observation is important because it shows the material property which appears as the consequence of QD regular ordering. A similar effect was for the first time observed in metallic QD superlattices and it was characterized as the first intrinsic properties of fcc supercrystals.[50,51]

VI. DISCUSSION

The $(Ge+SiO_2)/SiO_2$ multilayer films deposited at 500 °C and annealed at different temperatures are analyzed by several comparative experimental techniques. All applied techniques give evidence of the formation of QD superlattices in amorphous silica matrix. STEM and GISAXS measurements show formation of the dots and their ordering in a rhombohedral lattice with a substantial degree of order. The excellent statistics of GISAXS measurements allows us to determine precisely the superlattice unit cell parameters and the degree of the disorder of the dot lattice; these parameters cannot be obtained from local methods such as STEM. Furthermore, GISAXS technique is very sensitive to degree of dots regular ordering in 3D lattice. Using GISAXS method we can precisely determine degree of in-layer and interlayer correlation in dots positions.

GISAXS was also used for the characterization of the mean dot shape. The dots are found to be elongated and tilted in respect to substrate surface for annealing temperatures below 800 °C, while they are spherical for 800 °C or higher. However, GISAXS cannot resolve the inner structure of dots, it cannot distinguish amorphous and crystalline QDs and it is completely insensitive to lattice defects such as stacking faults or twins. Those properties are found from comparative HRTEM, SAED, and Raman analysis.

From all the methods used it follows that the structure of QDs evolves continuously with increasing annealing temperature. In particular, from an amorphous atomic structure found in the AS films to a completely crystalline one in the films annealed at 800 °C. As shown by all methods mentioned, the crystalline dots comprised pure germanium, with the diamond crystal lattice as in Ge bulk. There are some indications that lattice parameters of the dot lattice are slightly different than in Ge bulk based on Raman and SAED data,[32] but an additional diffraction analysis should be carried out to prove this hypothesis.

The observed enhancement of LFR intensity for the spatially ordered dot arrays indicates a collective vibrational behavior of the dots. As is shown in Refs. 50 and 51 van der Waals bonding of the QDs is sufficient to establish a correlation between the vibrating QDs, so they vibrate coherently resulting in oscillation eigenmodes of the QD superlattice. Because of weak bonding, all eigenmodes have the same frequency and enhancement of intensity occurs.

The dot growth is successfully explained and simulated by a simple growth model. The model is constructed as a combination of two mechanisms; each of them is separately experimentally confirmed to be efficient. We have shown that their combination can explain the self-ordering mechanism and the experimentally observed growth of the dots. The simulation efficiently describes the experimentally observed dot stacking in a rhombohedral lattice as well as the presence of certain degree of disorder, the latter depending on the number of deposited layers. The model also predicts different growth types for different deposition conditions. A more detailed investigation of the influence of the growth and annealing temperatures on the dot ordering, showing the formation of dots lattices with different degree of dots correlations as well as the experimental evidences for characterizing them, is presented separately.[32]

The growth simulations are made using three deposition parameters: the disorder degree (parameter $\sigma_{\|\|}$) that is determined by diffusion properties only, i.e., without substrate morphology effects; surface morphology properties induced by the formation of QDs in the underlayer (parameter b), and the degree of influence of the morphology of layers below on the morphology of the actually growing layer (parameter C). The advantage of such a description consists in its simplicity and generality. However, these parameters are purely phenomenological so that their connection to the "true" characteristics of the deposition process (diffusion rates, deposition temperature, activation energy of adatom diffusion, etc.) is rather indirect. For a full description of the growth by a kinetic Monte Carlo simulation, the true characteristics should be used. Nevertheless, the presented model well describes the basic experimentally observed properties of the QD growth in amorphous multilayers.

VII. SUMMARY

Structural properties of Ge quantum-dot arrays in amorphous SiO_2 grown by magnetron sputtering have been stud-

ied by small-angle x-ray scattering, transmission electron microscopy, and Raman scattering. The experimental data demonstrated that a self-organizing mechanism results in the spontaneous formation of rhombohedral quantum-dot crystals. A detailed analysis of x-ray scattering data by means of a numerical modeling based on a paracrystal model revealed the dependence of the ordering degree on the growth and annealing temperatures.

In contrast to quantum-dot arrays in a single crystalline matrix, where the ordering is caused by the elastic anisotropy of the host lattice, the ordering mechanism in amorphous SiO_2 is different; we have proved by a Monte Carlo simulation and comparison with experimental data that the ordering is induced by the influence of the surface morphology of adatom diffusion. The proposed growth model enables us to predict the optimum experimental conditions for a self-ordered growth of such multilayered systems.

ACKNOWLEDGMENTS

This work was supported by the Ministry of Science, Croatia. The authors are grateful to Medeja Gec for preparing samples for STEM and HRTEM measurements and Aleksa Pavlešin for assistance during the sample preparation. We wish to thank Dunja Desnica-Frankovič for critically reading the manuscript and discussions. V.H. acknowledges the support from the Ministry of Education of the Czech Republic (Project. No. MSM 0021620834) and G.D. acknowledges the support of the Slovenian Research Agency (Grant No. P2-0084).

[1] Q. Xie, A. Madhukar, P. Chen, and N. P. Kobayashi, Phys. Rev. Lett. **75**, 2542 (1995).
[2] J. Tersoff, C. Teichert, and M. G. Lagally, Phys. Rev. Lett. **76**, 1675 (1996).
[3] G. Springholz, V. Holý, M. Pinczolits, and G. Bauer, Science **282**, 734 (1998).
[4] J. Stangl, V. Holý, and G. Bauer, Rev. Mod. Phys. **76**, 725 (2004).
[5] G. Springholz, C. R. Phys. **6**, 89 (2005).
[6] E. V. Shevchenko, D. V. Talapin, N. A. Kotov, S. O'Brien, and C. B. Murray, Nature (London) **439**, 55 (2006).
[7] M. Elhassan, R. Akis, J. P. Bird, D. K. Ferry, T. Ida, and K. Ishibashi, Phys. Rev. B **70**, 205341 (2004).
[8] O. L. Lazarenkova and A. A. Balandin, Phys. Rev. B **66**, 245319 (2002).
[9] T. Kimura, H. Tamura, K. Kuroki, K. Shiraishi, H. Takayanagi, and R. Arita, Phys. Rev. B **66**, 132508 (2002).
[10] A. P. Alivisatos, Science **271**, 933 (1996).
[11] A. Konchenko, Y. Nakayama, I. Matsuda, S. Hasegawa, Y. Nakamura, and M. Ichikawa, Phys. Rev. B **73**, 113311 (2006).
[12] Y. Nakayama, I. Matsuda, S. Hasegawa, and M. Ichikawa, Appl. Phys. Lett. **88**, 253102 (2006).
[13] D. V. Talapin and C. B. Murray, Science **310**, 86 (2005).
[14] K. Karrai, R. J. Warburton, Ch. Schulhauser, A. Högele, B. Urbaszek, E. J. McGhee, A. O. Govorov, J. M. Garcia, B. D. Gerardot, and P. M. Petroff, Nature (London) **427**, 135 (2004).
[15] M. Perrini, S. Barbay, M. Brambilla, and R. Kuszelewicz, Appl. Phys. B: Lasers Opt. **81**, 905 (2005).
[16] M. Kroutvar, Y. Ducommun, D. Heiss, M. Bichler, D. Schuh, G. Abstreiter, and J. J. Finley, Nature (London) **432**, 81 (2004).
[17] C. Bostedt, T. van Buuren, T. M. Willey, N. Franco, and L. J. Terminello, Appl. Phys. Lett. **84**, 4056 (2004).
[18] Y. Maeda, Phys. Rev. B **51**, 1658 (1995).
[19] S. K. Ray, Opt. Mater. (Amsterdam, Neth.) **27**, 948 (2005).
[20] D. Riabinina, Ch. Durand, M. Chaker, N. Rowell, and F. Rosei, Nanotechnology **17**, 2152 (2006).
[21] J. K. Shen, X. L. Wu, C. Tan, R. K. Yan, and X. M. Bao, Phys. Lett. A **300**, 307 (2002).
[22] A. Dowd, R. G. Elliman, M. Samoc, and B. Luther-Davies, Appl. Phys. Lett. **74**, 239 (1999).
[23] Q. Xu, I. D. Sharp, C. W. Yuan, D. O. Yi, C. Y. Liao, A. M. Glaeser, A. M. Minor, J. W. Beeman, M. C. Ridgway, P. Kluth, J. W. Ager, D. C. Chrzan, and E. E. Haller, Phys. Rev. Lett. **97**, 155701 (2006).
[24] A. Kanjilal, J. Lundsgaard Hansen, P. Gaiduk, A. Nylandsted Larsen, N. Cherkashin, A. Claverie, P. Normand, E. Kapelanakis, D. Skarlatos, and D. Tsoukalas, Appl. Phys. Lett. **82**, 1212 (2003).
[25] T. C. Chang, S. T. Yan, P. T. Liu, C. W. Chen, S. H. Lin, and S. M. Sze, Electrochem. Solid-State Lett. **7**, G17 (2004).
[26] D. J. Eaglesham and M. Cerullo, Phys. Rev. Lett. **64**, 1943 (1990).
[27] C. Teichert, Phys. Rep. **365**, 335 (2002).
[28] U. Pietsch, V. Holý, and T. Baumbach, *High-Resolution X-Ray Scattering* (Springer-Verlag, New York, 2004).
[29] M. Zacharias and P. Streitenberger, Phys. Rev. B **62**, 8391 (2000).
[30] J. Li, X. L. Wu, D. S. Hu, Y. M. Yang, T. Qiu, and J. C. Shen, Solid State Commun. **131**, 21 (2004).
[31] S. Foss, T. G. Finstad, A. Dana, and A. Aydinli, Thin Solid Films **515**, 6381 (2007).
[32] M. Buljan, U. V. Desnica, G. Drazić, M. Ivanda, N. Radić, P. Dubček, K. Salamon, S. Bernstorff, and V. Holý, Nanotechnology (to be published).
[33] D. Babonneau, F. Petroff, J.-L. Maurice, F. Fettar, and A. Vaurès, Appl. Phys. Lett. **76**, 2892 (2000).
[34] D. Thiaudière, O. Proux, J.-S. Micha, C. Revenant, J.-R. Regnard, and S. Lequien, Physica B **283**, 114 (2000).
[35] J. R. Levine, J. B. Cohen, Y. W. Chung, and P. J. Georgopoulos, J. Appl. Crystallogr. **22**, 528 (1989).
[36] M. P. Tate, V. N. Urade, J. D. Kowalski, T. Wei, B. D. Hamilton, B. W. Eggiman, and H. W. Hillhouse, J. Phys. Chem. B **110**, 9882 (2006).
[37] R. Hosemann and S. N. Bagchi, *Direct Analysis of Diffraction by Matter* (North-Holland, Amsterdam, 1962).
[38] C. Revenant, F. Leroy, R. Lazzari, G. Renaud, and C. R. Henry, Phys. Rev. B **69**, 035411 (2004).
[39] Z. Zhang and M. G. Lagally, Science **276**, 377 (1997).
[40] F. Ratto, A. Locatelli, S. Fontana, S. Kharrazi, S. Ashtaputre, S. K. Kulkarni, S. Heun, and F. Rosei, Phys. Rev. Lett. **96**, 096103

(2006).
[41] M. Fanfoni and M. Tomellini, J. Phys.: Condens. Matter **17**, R571 (2005).
[42] A. Karmous, I. Berbezier, and A. Ronda, Phys. Rev. B **73**, 075323 (2006).
[43] I. Berbezier, A. Karmous, P. D. Szkutnik, A. Ronda, A. Sgarlata, A. Balzarotti, P. Castrucci, M. Scarselli, and M. De Crescenzi, Mater. Sci. Semicond. Process. **9**, 812 (2006).
[44] R. P. Millane and J. L. Eads, Acta Crystallogr., Sect. A: Found. Crystallogr. **56**, 497 (2000).
[45] J. L. Eads and R. P. Millane, Acta Crystallogr., Sect. A: Found. Crystallogr. **57**, 507 (2001).
[46] M. Fujii, S. Hayashi, and K. Yamamoto, Jpn. J. Appl. Phys., Part 1 **30**, 687 (1991).
[47] H. Richter, Z. P. Wang, and L. Ley, Solid State Commun. **39**, 625 (1981).
[48] I. H. Campbell and P. M. Fauchet, Solid State Commun. **58**, 739 (1986).
[49] M. Ivanda, A. Hohl, M. Montagna, G. Mariotto, M. Ferrari, Z. Crnjak Orel, A. Turković, and K. Furić, J. Raman Spectrosc. **37**, 161 (2006).
[50] A. Courty, A. Mermet, P. A. Alboy, E. Duval, and M. P. Pileni, Nature Mater. **4**, 395 (2005).
[51] M. Brust, Nature Mater. **4**, 364 (2005).